JACS
JOURNAL OF THE AMERICAN CHEMICAL SOCIETY
Article
pubs.acs.org/JACS

Intimate Binding Mechanism and Structure of Trigonal Nickel(I) Monocarbonyl Adducts in ZSM-5 Zeolite—Spectroscopic Continuous Wave EPR, HYSCORE, and IR Studies Refined with DFT Quantification of Disentangled Electron and Spin Density Redistributions along σ and π Channels

Piotr Pietrzyk,*[,†] Tomasz Mazur,[†] Katarzyna Podolska-Serafin,[†] Mario Chiesa,[‡] and Zbigniew Sojka[†]

[†]Faculty of Chemistry, Jagiellonian University, ul. R. Ingardena 3, 30-060 Krakow, Poland

[‡]Dipartimento di Chimica, Università di Torino and NIS Centre of Excellence, via P. Giuria 7, 10125, Torino, Italy

Supporting Information

ABSTRACT: Interaction of tetracoordinated nickel(I) centers generated inside the channels of ZSM-5 zeolite with carbon monoxide (^{12,13}CO, p_{CO} < 1 Torr) led to the formation of T-shaped, top-on monocarbonyl adducts with a unique trigonal nickel core, supported by two oxygen donor ligands. The mechanism of the formation of the {Ni^{I}−CO}ZSM-5 species was accounted for by a quantitative molecular orbital correlation diagram of CO ligation. Detailed electronic and magnetic structure of this adduct was obtained from comprehensive DFT calculations, validated by quantitative reproduction of its continuous wave electron paramagnetic resonance (CW-EPR), hyperfine sublevel correlation (HYSCORE), and IR fingerprints, using relativistic Pauli and ZORA-SOMF/B3LYP methods. Molecular analysis of the stretching frequency, ν_{CO} = 2109 cm^{-1}, g and A(^{13}C) tensors (g_{xx} = 2.018, g_{yy} = 2.380, g_{zz} = 2.436, A_{xx} = +1.0 ± 0.3 MHz, A_{yy} = −3.6 ± 0.9 MHz, A_{zz} = −1.6 ± 0.3 MHz) and Q(^{27}Al) parameters (e^2Qq/h = −13 MHz and η = 0.8) supported by quantum chemical modeling revealed that the Ni−CO bond results from the π overlap between the low-laying π(2p) CO states with the $3d_{xz}$ and $3d_{yz}$ orbitals, with a small σ contribution due to the overlap of σ(2p+2s) orbital and a protruding lobe of the in-plane $3d_{xz}$ orbital. Two types of orbital channels (associated with the σ and π overlap) of the electron and spin density flows within the {Ni^{I}−CO} unit were identified. A bathochromic shift of the ν_{CO} stretching vibration was accounted for by resolving quantitatively the separate contributions due to the σ donation and π back-donation, whereas the ^{13}C hyperfine coupling was rationalized by incongruent α and β spin flows via the σ and π channels. As a result the very nature of the carbon−metal bond in the Ni^{I}−CO adduct and the molecular backbone of the corresponding spectroscopic parameters were revealed with unprecedented accuracy.

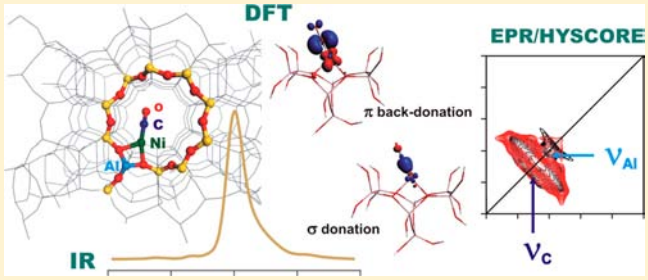

1. INTRODUCTION

Among catalyzed reactions, those involving carbon monoxide have recently been the subject of intensive investigations at both fundamental and applied levels.[1−6] They concern both coordination and organometallic chemistry[3,4,6] as well as heterogeneous catalysis. Selective catalytic reduction (SCR),[5] oxidation of CO,[7−9] methanol synthesis and CO hydrogenation,[10] or preferential oxidation of carbon monoxide in the presence of hydrogen (PROX reaction)[11,12] may serve here as examples. Because of high sensitivity of its stretching vibration to charge redistribution upon bonding, carbon monoxide is also widely used as an excellent probe molecule for characterization of the valence and coordination states of transition metals in zeolites,[13] supported oxides,[14] and also for probing local electrostatic field strength via the vibrational Stark effect.[15]

Nickel-exchanged zeolites have attracted increasing attention owing to their activity in deNO$_x$,[5,16] olefin dimerization[17] or carbon dioxide reforming of methane.[18] Nickel(I) carbonyls, in particular, are the key species involved in many enzymatic and catalytic processes.[19,20] For instance, homogeneous Ni^{I}-carbonyls of biologically relevant complexes can mimic the activity of acetylcoenzyme A (acetyl-CoA) synthases[21] or dihydrogen oxidation by hydrogenases.[22] Elucidation of reversible or irreversible character of carbon monoxide binding for these processes is of the key concern for such systems.[23] Low coordination number of the metal center and space confinement effects imposed by the framework on the intrazeolite nickel−carbonyl complexes, in turn, allow for studying their unique stereochemistry that is not easily obtainable in homogeneous conditions.

Vibrational description of the carbonyl coordination chemistry of dispersed nickel cations has been summarized

Received: June 11, 2013
Published: September 17, 2013

   dx.doi.org/10.1021/ja405874t | J. Am. Chem. Soc. 2013, 135, 15467−15478

elsewhere.[14] The carbonyl adducts with Ni^{2+} give rise to IR bands located at the 2220−2180 cm^{-1} region. They are destroyed at ambient temperature, probably because of the lack of stabilizing π back-donation, in contrast to much more stable CO adducts of monovalent nickel, observable in the 2160−2050 cm^{-1} region. It is usually argued that their enhanced stability is caused by the interplay between the σ and π electronic interactions, although these processes have not been quantified separately as yet.

Depending on the nature of the coligands, the carbonyl complexes of tricoordinated Ni^{I} can adopt a Y-shaped or a T-shaped geometry.[6,21,24] It has also been found that the Y or T conformations involve a significant difference in the electronic structure and reactivity of the three-coordinate complexes in ligand substitution and transmetalation reactions, constituting an essential factor in the structural and kinetic studies.[25,26] Therefore, taking into account a far reaching analogy between the intrazeolite and enzymatic congeners,[27] to comprehend the fundamental chemistry of the $\{Ni^{I}-CO\}$ unit for sensible control of its reactivity, a detailed molecular level description of its geometry, electronic and magnetic properties is of a great chemical value.

Among many methods applied to investigate the systems hosting the $\{Ni^{I}-CO\}$ adducts, electron paramagnetic resonance (EPR) and its related pulse variants are obviously the prime techniques of choice due to the paramagnetic nature of those species.[21] However, an in-depth interpretation of the EPR spectral parameters in terms of the molecular structure of the corresponding complexes is not a trivial task, taking into account an intricate nature of the magnetic interactions within the metal−ligand unit and the constraints imposed by low symmetry. Yet, because of the recent relativistic DFT methods, calculations of EPR parameters are becoming nowadays accessible even for larger systems containing transition metal ions.[28] The recent progress in this field has been reviewed by us elsewhere.[29] Calculations of the $\boldsymbol{g}$ tensor for nickel(I) complexes have focused so far mostly on biomimetic systems,[6,30] homogeneous complexes,[31,32] and paramagnetic Ni adducts with NO ligands.[33] It has been shown that conceptually useful results can also be obtained by analyzing simpler models such as $Ni^{I}(CO)_nL_m$ adducts (n = 1−4, L = H_2O, OH^-) epitomizing broad range of the conceivable chemical environments.[34] Having established the principal relationships between the electronic nature of the $\boldsymbol{g}$ and $\boldsymbol{A}$ tensors and the stereochemistry of the well-defined nickel−carbonyl model systems, they can be used as a convenient reference for analysis of the structurally more demanding real complexes.[35]

This paper is devoted to a detailed description of an electronic and magnetic structure of the monocarbonyl complexes with monovalent nickel produced by adsorption of CO at low pressures (p_{CO} < 1 Torr) on dehydrated, reduced Ni^{I}ZSM-5 zeolite. The occurrence, identification, and spectroscopic properties of di-, tri-, and tetracarbonyls, produced at higher CO pressures, will be discussed in a forthcoming paper. Herein, we investigated more closely the molecular nature of the $\boldsymbol{g}$ and ^{13}C hyperfine tensors of the $\{Ni^{I}-CO\}$ adducts in terms of the local symmetry and the coordination state of nickel, to provide a clear-cut evidence for their definite assignment. A frontier molecular orbital picture of CO ligation, quantification of the σ and π channels of electron and spin density redistribution upon bonding, and detailed insight into the magnetic molecular orbitals that contribute to the experimentally observed $\boldsymbol{g}$ tensor anisotropy were also discussed. The manuscript is organized as follows: (1) collection of the spectroscopic data, (2) confirmation of the stoichiometry of the monocarbonyl adduct from IR data, (3) local symmetry assignment, inspection of the nearest environment by EPR and hyperfine sublevel correlation (HYSCORE) probes, (4) development of the molecular model of the monocarbonyl adduct and determination of its electronic and magnetic structure with charge and spin resolution, (5) molecular insights into the nature of the Ni−CO bond and the related spectroscopic parameters through quantum chemical calculations.

2. MATERIALS AND METHODS

2.1. Materials. Ni-exchanged ZSM-5 metallozeolite was obtained by a standard ion exchange method using 0.1 M aqueous solution of $Ni(NO_3)_2$ and an ammonium form of the parent ZSM-5 zeolite (Zeolyst, Inc.) with the Si/Al ratio equal to 15. Final pH of the solution varied from 2 to 5. Chemical analysis by means of ICP-MS method revealed the Ni/Al exchange degree of 54%. After drying in air, prior to the spectroscopic measurements, the samples were activated in a vacuum of 10^{-5} mbar at 773 K for 2 h (with the heating rate of 6 K/min), reduced with CO (Aldrich, 99.95%) at 673 K for 30 min, and finally evacuated at 553 K. The monocarbonyl complexes were generated by exposure of the reduced samples to CO at low pressures (below 1 Torr). To ensure formation of the monocarbonyl species only, adsorption of CO at 298 K on the reduced Ni^{I}ZSM-5 sample was followed by careful evacuation of the samples monitored by continuous wave electron paramagnetic resonance (CW-EPR), to check the disappearance of the diagnostic features of possible spurious dicarbonyls (for spectroscopic signatures of both species, see Supporting Information). After such adsorption procedure, the EPR tube was sealed and disconnected from the adsorption cell to perform pulse EPR measurements.

2.2. Spectroscopic Methods. FTIR spectra were recorded on a Bruker Tensor 27 spectrometer equipped with MCT detector (at a spectral resolution of 2 cm^{-1}). The samples in a form of the self-supporting pellets were placed in an IR cell connected to a vacuum line for in situ thermal activation (773 K) followed by reduction in CO and subsequent evacuation. Adsorption of carbon monoxide was carried out at ambient temperature. All spectra were normalized to standard pellet mass (10 mg, density 3.2 mg/cm^2).

CW-EPR spectra were recorded at 77 K with a Bruker ELEXSYS-E580 X-band spectrometer using a rectangular TE_{102} cavity with the 100 kHz field modulation. The microwave power of 1−10 mW and the modulation amplitude of 0.1−0.5 mT were applied. Computer simulations of the spectra were performed with the EPRsim32 program,[36] which calculates exact solutions for the spin-Hamiltonian by full matrix diagonalization. A hybrid search procedure combining genetic algorithm and Powell refinement was applied for optimization of the simulated spectra.

Pulse EPR experiments were performed on a Bruker ELEXSYS-E580 spectrometer (at microwave frequency of 9.76 GHz) equipped with a liquid-helium cryostat from Oxford Instruments. All measurements were performed at 5−10 K. Electron spin echo (ESE) detected EPR spectra were obtained with the two-pulse sequence: $\pi/2-\tau-\pi-\tau-$echo with the microwave pulse lengths $t_{\pi/2}$ = 16 ns and t_π = 32 ns and the delay time τ = 200 ns. Hyperfine sublevel correlation (HYSCORE)[37] experiments were carried out with the four-pulse sequence: $\pi/2-\tau-\pi/2-t_1-\pi-t_2-\pi/2-\tau-$echo with the microwave pulse lengths $t_{\pi/2}$ = 16 ns and t_π = 16 ns. The time intervals t_1 and t_2 were varied with an increment of 16 ns starting from 96 ns up to 3296 ns. In order to avoid the blind-spot effects various τ values were chosen, and the obtained spectra were added up after Fourier transformation. An eight-step phase cycling was selected in order to eliminate unwanted echoes. The obtained HYSCORE spectra were baseline corrected, apodized with Hamming window, and zero filled. After a two-dimensional Fourier transformation, the absolute value

spectra were calculated, and next simulated with the EasySpin software.[38]

2.3. DFT Modeling. Zeolite sites, acting as the rigid multidentate mineral ligands for hosting the nickel(I) centers and nickel(I)−carbonyl adducts, were modeled using geometrically embedded clusters of various number of T-atoms (T = Si or Al). The clusters were cut off from a model of the MFI lattice (using Materials Studio, Accelrys), and the resulting dangling bonds were saturated with the hydrogen atoms. Those atoms were placed along the broken O−Si bonds at the equilibrium distance, and during the geometry optimization they were kept frozen in order to mimic the rigidity of the outer part of the ZSM-5 zeolitic framework. A cluster of the $[Si_6AlO_8(OH)_{12}]^-$ stoichiometry, referred to as **M7**, was used as a binding site for nickel ions, based on the previous experimental results[39] and DFT cluster modeling.[40−42] The results obtained for the additional **I3** and **M9** structures were deposited in Supporting Information to prove the convergence of the results obtained for the **M7** model.

Partial geometry optimization was carried out for the $Ni^I[Si_6AlO_8(OH)_{12}]$ and $[CO\text{-}Ni^I][Si_6AlO_8(OH)_{12}]$ models by means of the Gaussian09[43] software at the spin-unrestricted level. The B3LYP[44] exchange-correlation potential and all-electron basis set with additional polarization functions, denoted as 6-311G(d,p),[45] were used. The structure of the cluster models were optimized with the analytic gradients and Berny algorithm using GEDIIS method,[46] within the SCF electron density convergence criterion of 10^{-6} a.u., a maximum force criterion of 4.5×10^{-4} a.u./Å, and a maximum displacement criterion of 1.8×10^{-3} Å. Vibrational analysis was carried out within the harmonic approximation with the second derivatives computed numerically (two steps with 0.001 Å).

Electron density redistribution upon CO bonding (quantification of the σ and π donation effects) and population analysis was performed on the basis of the natural orbitals for chemical valence technique combined with the Ziegler−Rauk extended transition state energy decomposition scheme (ETS-NOCV)[47,48] as implemented in the ADF program suite (version 2009.01).[49,50] The ETS-NOCV analysis allows for separation and quantification of the electron density transfer channels between the intentionally delineated interacting fragments, for example, $[CO]_{frag}$ and $[Ni^I\mathbf{M7}]_{frag}$. In such a case the pairs of the natural orbitals for chemical valence (Ψ_{-k},Ψ_k) allow for factorization differential charge density, $\Delta\rho$, into the particular NOCV contributions $(\Delta\rho_k)$:[47]

$$\Delta\rho(r) = \sum_{k=1}^{M/2} \nu_k[-\psi_{-k}^2(r) + \psi_k^2(r)] \quad (1)$$

where ν_k and M stand for the NOCV eigenvalues and the number of basis functions, respectively. For the open-shell systems the summation of the α and β electron densities must be carried out separately over the spin−orbitals of virtually the same symmetry, but not necessarily possessing the same ν_k values as shown previously by us for the $\{Ni^{II}-O_2^-\}$ZSM-5 system.[27]

The $\boldsymbol{g}$ tensor values were calculated using the ORCA software.[51] The scalar relativistic zeroth-order regular approximation (ZORA) corrections were applied for the electron structure calculations, whereas the mean-field approximation (SOMF),[52] including both the spin−own-orbit and spin−other-orbit interactions in the exchange term, was used for accounting for the spin−orbit coupling (SOC) effects. In addition, the one-component approach due to Schreckenbach and Ziegler[53] was applied for construction of the molecular magnetic field-induced coupling diagrams based on the Pauli Hamiltonian (implemented in the ADF program). The hyperfine coupling $\boldsymbol{A}$ tensor and the quadrupole parameters were calculated according to the spin-density based formulation that in the case of the hyperfine interaction includes additionally the SOC contribution as a second-order property.[54] For the spectroscopic calculations the B3LYP hybrid functional with the all-electron triple-ζ basis sets was used for all atoms except of nickel, where a more accurate CP(PPP)[55] basis set was employed.

3. RESULTS AND DISCUSSION

3.1. Structure of Parent Nickel(I) Sites. The monovalent nickel(I) sites in ZSM-5 channels were produced by reduction of nickel-oxo species with CO at 673 K (Ni(II)−O−Ni(II) + CO → 2Ni(I) + CO_2) followed by prolonged evacuation of the reduced samples at 553 K. The diagnostic well resolved nearly axial EPR spectrum of Ni(I) with $g_{zz} > g_{xx,yy}$ is shown in Figure 1a. As discussed in our previous paper in more detail,[27] it

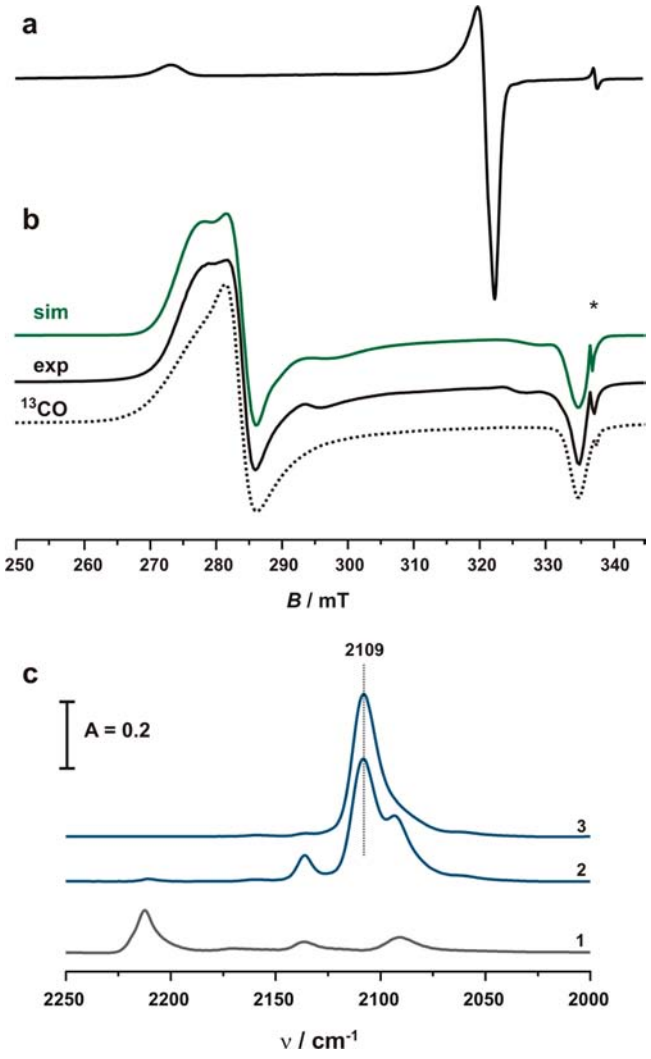

Figure 1. X-band CW-EPR spectra (77 K) of (a) reduced Ni^IZSM-5 zeolite after prolonged evacuation, (b) after adsorption of ^{12}CO (p_{CO} < 1 Torr) and formation of nickel(I) monocarbonyls (dotted line corresponds to ^{13}CO adsorption). The asterisk indicates an isotropic signal due to thermally induced framework defect. (c) FTIR spectra (ambient temperature) of ^{12}CO adsorption on (1) thermally activated Ni^{II}ZSM-5, after reduction in CO (620 K) and subsequent evacuation at (2) 320 K and (3) 350 K leading finally to formation of sole monocarbonyl species of nickel(I).

consists of a dominant signal due to the isolated tetracoordinated nickel(I) center with $g_{xx} = g_{yy} = 2.098$, $g_{zz} = 2.478$, determined by computer simulation. An expected anisotropy in the $x-y$ plane is, however, barely manifested in the experimental X-band spectrum because of the linewidths broadening. Such rhombic distortion of the $\boldsymbol{g}$ tensor would be consistent with a rectangular deformation of the 4-fold arrangement of the planar donor $O_{(Al,Si)}$ ligands (C_{2v}

dx.doi.org/10.1021/ja405874t | J. Am. Chem. Soc. 2013, 135, 15467−15478

symmetry), caused by the presence of an Al atom in the 12-membered macrocyclic ring of the zeolite framework. The corresponding Ni−$O_{(Si,Si)}$ bond lengths are equal to 2.236 and 2.202 Å, whereas the Ni−$O_{(Al,Si)}$ bond lengths are equal to 2.105 and 2.115 Å (Figure 2a). The composition of the singly occupied molecular orbital (SOMO), $|SOMO\rangle = 0.83|3d_{x^2-y^2}\rangle + 0.12|3d_{yz}\rangle + 0.03|3d_{z^2}\rangle + 0.01|3d_{xz}\rangle$, accounts well for the dominant axial component of the g tensor, whereas the weak rhombic component is associated with the appreciable admixture of the $|3d_{yz}\rangle$ state. The calculated (ZORA-SOMF/B3LYP) g tensor values (g_{xx} = 2.117, g_{yy} = 2.153 and g_{zz} = 2.324) remain in a good agreement with their experimental counterparts.[27]

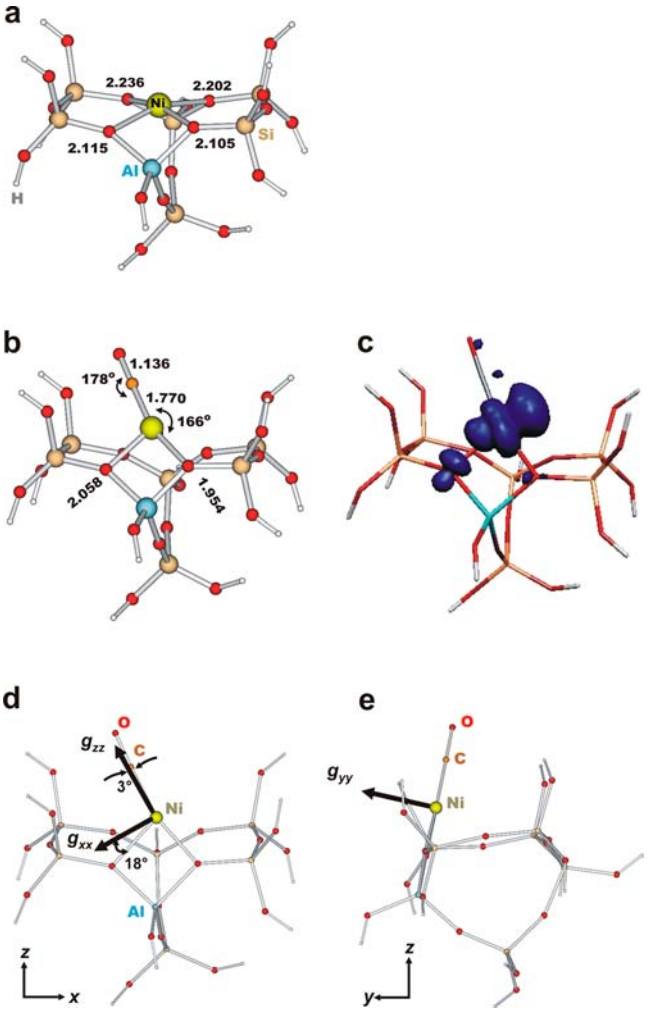

Figure 2. (a) DFT optimized structures of the Ni^{I}**M7** cluster, (b) {Ni^{I}−CO}**M7** cluster, (c) corresponding spin density contour of the monocarbonyl adduct, and (d, e) orientation of the principal axes of the g tensor with respect to the molecular framework. Bond lengths are given in Angstroms, and angles in degrees.

3.2. Binding of CO to Ni(I) Sites. The planar structure of the parent intrazeolite $Ni^{I}(O_{(Si,Al)})_4$ sites is comparable to the coordination environment of nickel in the homogeneous complexes with tetradentate supporting ligands[56] and nickel enzymes.[21] Thus, similar EPR spectra of the Ni(I) centers have also been observed. Favorable spatial and energetic accessibility of the nickel orbitals, controlled by weak oxygen donor ligands ($O_{(Si,Al)}$) of the zeolite matrix, makes capture of CO molecules quite easy. Indeed, adsorption of ^{12}CO at 298 K (under the pressure below 1 Torr) on the reduced Ni^{I}ZSM-5 sample led to the development of a new well resolved orthorhombic EPR signal shown in Figure 1b, together with its computer simulation (green line). The obtained g tensor values are equal to g_{xx} = 2.018, g_{yy} = 2.380, g_{zz} = 2.436. Analogous experiment with isotopically labeled ^{13}CO (I = 1/2, 90%) did not lead to appearance of any resolved superhyperfine structure due to ^{13}C nuclear spin, and a merely appreciable line broadening indicated that the spin density is essentially retained on the nickel center upon CO attachment. This point was further elucidated by means of HYSCORE spectroscopy (vide infra). The corresponding IR spectra (Figure 1c) recorded in similar conditions revealed formation of an intense band at ν_{CO} = 2109 cm^{-1} characteristic of the C−O stretching vibration (the accompanying bands at 2136 and 2091 cm^{-1} are due to the dicarbonyl species, whereas the band at 2212 cm^{-1} in Ni^{II}ZSM-5 sample results from the Ni^{II}−CO adducts).[57] A bathochromic shift of this band with respect to the gas phase, $\Delta\nu$ = −34 cm^{-1}, indicates domination of the π back-donation over the σ donation effects, discussed below in more detail. On the basis of the g tensor and ν_{CO} signatures, the observed adduct can be assigned to the covalently bound monocarbonyl nickel(I) species.[13,57,58] All those experimental facts indicate clearly that in the case of the {Ni^{I}−CO}ZSM-5 system the nickel core remains monovalent upon CO ligation. Although the monocarbonyl species are quite stable, they can be destroyed after prolonged evacuation at elevated temperatures, yielding bare Ni(I) sites.

The observed g tensor anisotropy and symmetry of the EPR signal can be used for assigning the coordination mode of the {Ni^{I}−CO} monocarbonyl. As already mentioned, it can assume one of the generic T or Y conformations known from the bioinorganic complexes, where the nickel(I) core remains three-coordinated.[6,21,24] As shown earlier, the g tensor is sensitive to the conformation type and the resulting ground

Table 1. Experimental and DFT-Calculated Spectroscopic Parameters, Frequency of the CO Vibration, ν_{CO}, g Tensor, ^{13}C Hyperfine Tensor, A, and Orientation of the Principal Axes of the $A(^{13}C)$ Tensor with Respect to the g Tensor Axes for the Ni^{I}−CO Adducts in ZSM-5 Zeolite[a]

spectroscopic parameters	experimental values			DFT-calculated values		
ν_{CO}/cm^{-1}	2109			2102		
g tensor g_{xx}, g_{yy}, g_{zz}	2.018 ± 0.001	2.380 ± 0.005	2.436 ± 0.005	2.016	2.224	2.433
^{13}C hyperfine tensor A_{xx}, A_{yy}, A_{zz}/MHz	+1.0 ± 0.3	−3.6 ± 0.9	−1.6 ± 0.3	+5.9	−9.4	−4.9
Euler angles[b] (^{13}C)A tensor α, β, γ/deg	0	84 ± 10	0	0	80	−2

[a]Calculated magnetic parameters for ^{27}Al nucleus are listed in Table S2 (Supporting Information) along with the corresponding simulated HYSCORE patterns. [b]Euler rotations are defined assuming first rotation by α around z-axis, second rotation by β around y'-axis, and finally third rotation by γ around z''-axis.

dx.doi.org/10.1021/ja405874t | J. Am. Chem. Soc. 2013, 135, 15467−15478

state,[24] which allows for a clear-cut assignment of the observed {Ni^{I}−CO} adduct in ZSM-5 to the T conformation with the predominant 3d$_{xz}$ SOMO, consistent with the observed sequence $g_{zz} > g_{yy} \gg g_{xx}$ of the g values (Table 1). This order of the g_{ii} components discards simple apical CO binding to 4-fold nickel(I) preserving its parent coordination to the zeolite framework, since in such a case the expected ground state would result in the $g_{xx} \sim g_{yy} \ll g_{zz}$ sequence.[34]

To determine the hyperfine splitting due to ^{13}CO, unresolved in the simple CW-EPR experiments, and to ascertain the coordination environment of the {Ni^{I}−CO} magnetophore hosted in the ZSM-5 zeolite, a number of pulse EPR measurements were carried out. At first, an electron spin echo (ESE) detected EPR spectrum of the nickel(I) monocarbonyl was recorded (Figure 3), the first derivative of

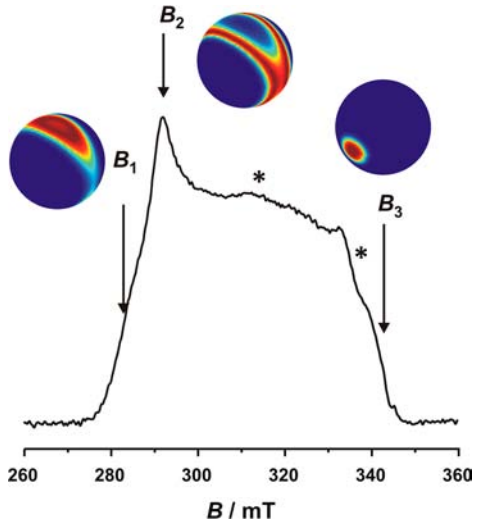

Figure 3. Echo-detected EPR spectrum of {Ni^{I}−^{12}CO}ZSM-5 monocarbonyl adduct ($\pi/2$ = 16 ns, τ = 200 ns, T = 10 K). The arrows indicate the observer positions B_1 = 282.5 mT, B_2 = 292.0 mT, and B_3 = 342.0 mT at which HYSCORE spectra were recorded, whereas the unit spheres show orientation selectivity for the particular observer positions (red shadings indicate orientations on resonance with the microwave pulse, blue shadings off-resonance). The asterisks indicate weak features due to nickel(I) dicarbonyl species.

which closely resembles the corresponding CW-EPR spectrum shown in Figure 1b. The weak features indicated by the asterisks are due to the residual nickel(I) dicarbonyl species, as definitely revealed in separate CW-EPR experiments, recorded with increasing CO pressures (see Supporting Information). The ESE spectrum was used for selection of the magnetic field observer positions (B_1, B_2, and B_3) corresponding to the principal orientations of the $\boldsymbol{g}$ tensor at which the HYSCORE experiments were next carried out. Taking the $\boldsymbol{g}$ tensor values derived from computer simulation of the powder CW-EPR spectra (Table 1), the computed orientation selection on the unit sphere (Figure 3) shows that at the field position B_3 only the species with the g_{xx} axis oriented along or close to the magnetic field contribute to the measurement. This orientation selective excitation allows for determination the magnetic interactions missing in CW-EPR (hyperfine and quadrupole couplings), with respect to the $\boldsymbol{g}$ tensor coordinate system. The unit sphere calculated for the observer position B_2, corresponding to the g_{yy} axis, shows that many orientations in the g_{yy}−g_{zz} plane of the {Ni^{I}−CO} species are in resonance with the microwave pulse, and jointly contribute to the measurement. Even though that the B_1 orientation seems to be more selective than the B_2 one, the highest intensity of the echo obtained for the latter position favored performing the HYSCORE experiments at the magnetic field set at B_2.

In HYSCORE experiments a correlation of nuclear frequencies in one electron spin (m_S) manifold with nuclear frequencies in the other manifold is created by means of a mixing π pulse. In the particular case of the {Ni^{I}−^{13}CO}ZSM-5 paramagnets, the hyperfine interactions are expected for ^{13}C nuclei (I = 1/2, ν_C = 3.748 MHz) of the adsorbed CO and ^{27}Al (I = 5/2, ν_{Al} = 3.886 MHz) atoms of the alumino-silicious framework (zeolite). Given the similarity of the Larmor frequencies ν (calculated for 350.0 mT) of these two nuclei, the HYSCORE spectra were recorded for both {Ni^{I}−^{12}CO}-ZSM-5 and {Ni^{I}−^{13}CO}ZSM-5 systems.

In the case of the {Ni^{I}−^{12}CO} isotopomer, the HYSCORE spectrum taken at the field position corresponding to B_2 (292.0 mT) shows an intense peak on the (+,+) quadrant diagonal at (ν_{Al}, ν_{Al}) amenable to the interaction with at least one ^{27}Al nucleus (Figure 4a). Recording the spectrum at the position B_3 (342.0 mT) reveals the presence of multiple diagonal peaks (Figure 4d) with considerable shift with respect to the ^{27}Al nuclear Larmor frequency. This can be explained considering a fairly large quadrupole interaction. Indeed, literature values ranging from 11 to 16 MHz have been reported for ^{27}Al in ZSM-5 and similar systems (faujasite, mordenite).[59,60] DFT computed values (vide infra) predict a quadrupole coupling of 13 MHz in line with these results. (The latter is characteristic of {Ni^{I}−CO}**M7**, whereas for a more extended {Ni^{I}−CO}**M9** model slightly reduced value of 10 MHz was obtained. For further discussion of the quadrupole interaction, see Supporting Information). The poor resolution of the HYSCORE spectra and the large number of parameters (9) that concur to determine the HYSCORE spectrum of ^{27}Al hamper the experimental determination of the full interacting tensors; however, simulation of the HYSCORE spectra carried out using the DFT predicted values for the ^{27}Al interactions (Table S2, Supporting Information) provide a reasonable reproduction of the main spectral features (Figure S2, Supporting Information). This, in turn, provides a valuable background for development of a confident model of the investigated adduct, and subsequent in-depth interpretation of the spectroscopic data with help of much more wide-ranging DFT results.

When ^{13}CO (I = 1/2, 90%) was used, a new ridge centered at the ^{13}C nuclear Larmor frequency was observed upon setting the magnetic field at the position B_2 (Figure 4b), which was not present in the case when ^{12}CO was used (Figure 4a). Recording the spectrum at the magnetic field equivalent to the g_{xx} component (the position B_3 in Figure 3) led to a single crystal-like spectrum (Figure 4e), characterized by two peaks centered at the Larmor frequency of ^{13}C. These signals are unambiguously assigned to the superhyperfine interaction between the unpaired electron, localized on the Ni 3d$_{xz}$ orbital, and the ^{13}C nucleus of the CO ligand. The maximum ridge extension of approximately 4 MHz, measured parallel to one of the axes in the spectrum in Figure 4b, corresponds to the maximum hyperfine coupling (A_{max}). Moreover, the ^{13}C ridge is clearly shifted from the (ν_C, ν_C) value, revealing a substantial dipolar interaction. Simulation of the spectra at two different magnetic field settings allows for determining the full ^{13}C hyperfine tensor, which is reported in Table 1. The individual patterns due to the contribution of the ^{13}C nucleus are shown

dx.doi.org/10.1021/ja405874t | J. Am. Chem. Soc. 2013, 135, 15467−15478

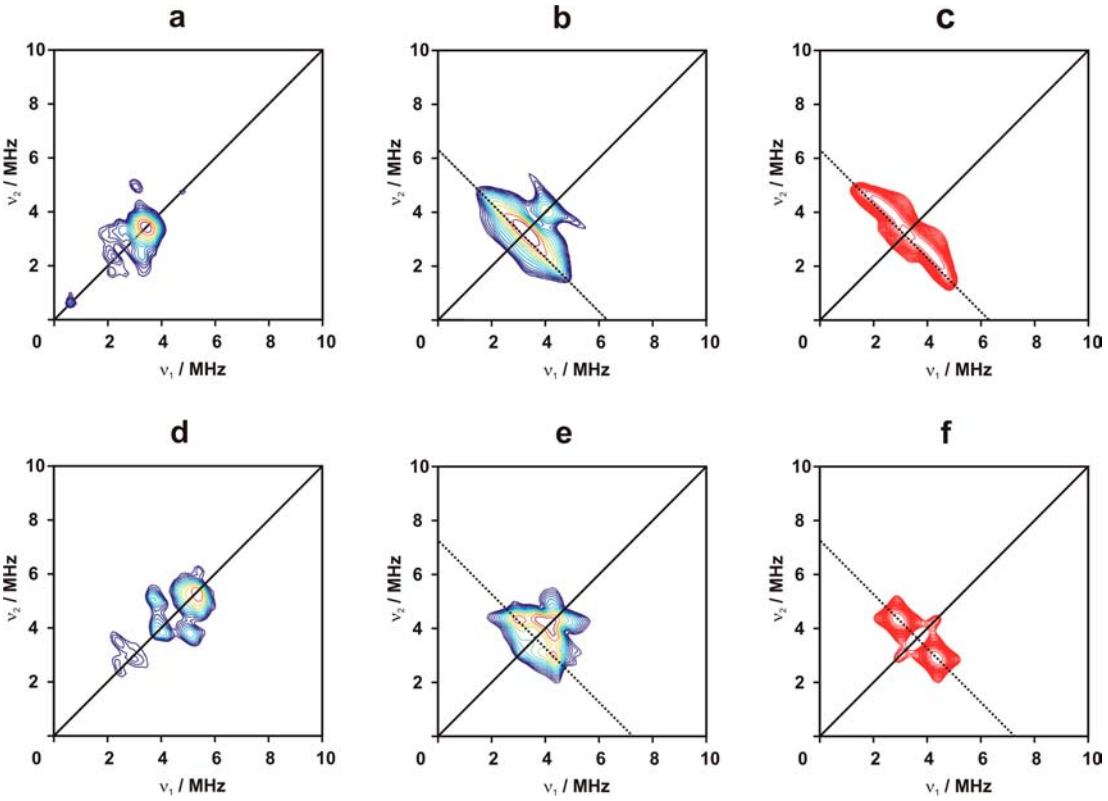

Figure 4. HYSCORE spectra of (a, d) {Ni^{I}−^{12}CO}ZSM-5 and (b, e) {Ni^{I}−^{13}CO}ZSM-5 systems taken at the observer positions B_2 = 292.0 mT (top) and B_3 = 342.0 mT (bottom) at 5 K with τ = 112 and 128 ns, and 0.75 kHz repetition rate. For the simulated HYSCORE patterns (c, f) only hyperfine interaction due to one ^{13}C (I = 1/2) nucleus was considered. Dotted lines indicate Larmor frequency of ^{13}C for each magnetic field value. For simulation of the ^{27}Al contribution, see Supporting Information (Figures S2, S3).

in Figure 4c,f. It should be noted that in the simulations the contributions of remote ^{27}Al and ^{13}C nuclei were neglected. This explains the slightly different shape in the experimental and simulated ridges.

The resulting ^{13}C hyperfine tensor is highly dipolar in nature with the maximum coupling oriented along the "perpendicular" g_{yy} component (note almost $\pi/2$ rotation of the A_{ii} and g_{ii} principal axes along the y direction, Table 1). Conventional decomposition of the $\boldsymbol{A}(^{13}\mathrm{C})$ tensor ($\boldsymbol{A} = a_{iso}\boldsymbol{I} + \boldsymbol{T}$) leads to $[\boldsymbol{T}]_{ii}$/MHz = [+2.4; −2.2; −0.2] and a_{iso}= −1.4 MHz, in accordance with the positive principal value of the dipolar coupling for 2p orbitals and positive g_n value for ^{13}C nucleus.[61] The negative isotropic constant is in agreement with the B3LYP calculations (a_{iso} = −2.8 MHz), and its origin is well accounted for by asymmetric α and β electron density flows within the {Ni^{I}−CO} moiety, discussed below in detail. The very small values of the ^{13}C hyperfine parameters suggest either a distal ligand−metal coordination (for instance an inverted Ni^{I}−OC bond) or minute delocalization of the spin density onto the CO ligand in the typical Ni^{I}−CO coordination. Since the $\boldsymbol{A}(^{13}\mathrm{C})$ tensor exhibits a predominant dipolar through-space nature, we verified the self-consistency of the HYSCORE spectra simulation with the proposed molecular model of the {Ni^{I}−CO} adduct using the estimation of the dipolar coupling based on the separate (diffuse) dipole approximation.[62] In this approach the maximal hyperfine splitting, A_{max}, can be associated with the Ni−C bond length, R, using the following formula:

$$A_{max} = g\mu_B g_n \mu_n \left[\frac{2R^2 - r^2}{2(R^2 + r^2)^{5/2}} + \frac{(R - r)^3 + (R + r)^3}{2(R + r)^3(R - r)^3} \right] \quad (2)$$

where r indicates the most probable distance of the unpaired electron from the nickel nucleus. For 3d states it can be approximated as $6a_0/Z^*$ (a_0 = 0.52918 Å), where the effective atomic number was calculated using the Slater rules: Z^* = 7.2 (for 3d^9 electron configuration). Taking R = 1.77 Å obtained from the DFT geometry optimization (see below) and uncertainty of the r value of ±0.1 Å, upon substituting the numerical values A_{max} = 4.9 ± 0.8 MHz was obtained, in reasonable agreement with the extent of the ^{13}C ridge (Figure 4b,c, Table 1), taking into account inherent approximations of both approaches.

The very small spin density transfer toward the CO ligand is at first glance surprising, in view of a pronounced metal-to-ligand π back-donation revealed by the sizable ($\Delta\nu$ = −34 cm^{-1}) red shift of the CO stretching frequency. In order to clarify this conundrum, and to develop a detailed self-consistent description of the electronic and molecular structure of the monocarbonyl complex, corroborative DFT calculations were carried out.

3.3. Electronic Structure and Binding Mechanism of {Ni^{I}−CO}. DFT calculations revealed that the {Ni^{I}−CO}**M7** adduct exhibits a moderately strong η^1 binding of the CO molecule (Figure 2b) with ΔE_{int} = −39 kcal/mol. The planar 3-fold coordination around the nickel center is featured by the top-on ligated CO moiety, with the distance to the metal center of 1.770 Å, and two longer Ni−O$_{(Al)}$ bonds with the zeolite

dx.doi.org/10.1021/ja405874t | J. Am. Chem. Soc. 2013, 135, 15467−15478

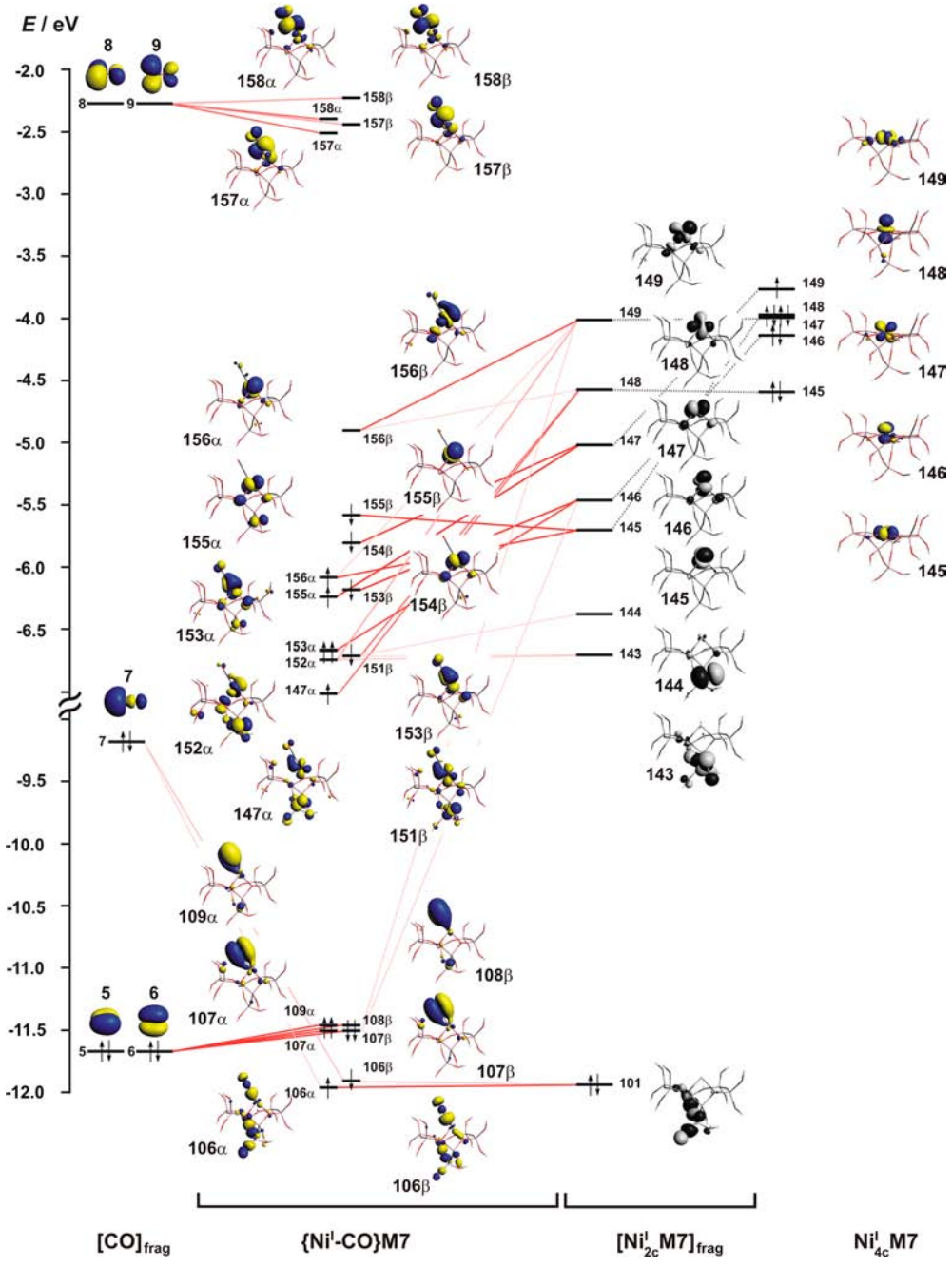

Figure 5. The Kohn–Sham frontier orbital interaction diagram for the {Ni^{I}–CO}**M7** model complex.

framework equal to 2.058 Å and 1.954 Å. The C–O bond length is elongated to 1.136 Å upon bonding with respect to the free $CO_{(g)}$ molecule (1.127 Å), and the $O_{(Al)}$–Ni–C angle of 166° nicely corroborates the T-conformation deduced from the analysis of the experimental ***g*** tensor. Such adsorption mode results in the trigonal (OC)–Ni^{I}–$(O_{(Al)})_2$ geometry and is characteristic of the constraint (entatic) environments such as enzyme prosthetic groups[6,19,21] or intrazeolite hosting sites.[2] Binding via the aluminum tetrahedron to zeolite framework explains the observed HYSCORE patterns due to ^{27}Al quadrupole interaction and a large value of the interaction parameters, $e^2qQ/h = -13$ MHz, $\eta = 0.8$, calculated within the ZORA-SOMF/B3LYP scheme (Supporting Information, Table S2 and S4).

The revealed T-conformation of the monocarbonyl adduct gives rise to the spin density distribution essentially confined to the nickel core (Figure 2c). The orientation of the principal axes of the ***g*** tensor with respect to the molecular framework of the {Ni^{I}–CO}**M7** complex is shown in Figure 2d,e. In agreement with the local C_s point symmetry of the (OC)–Ni^{I}–$(O_{(Al)})_2$ unit, the principal axes of the ^{13}C hyperfine tensor are noncollinear with the ***g*** tensor axes in the *xz* plane. They are rotated nearly about $\beta = 90°$ along the *y* direction (Table 1), giving rise to a monoclinic EPR spectrum.

The intimate nature of CO binding to the intrazeolite Ni(I) sites was examined in more detail with the help of a frontier molecular orbital (FMO) interaction diagram of the constituting molecular fragments. The latter are defined by the carbon monoxide ligand, $[CO]_{frag}$, the tetracoordinated nickel(I) site

dx.doi.org/10.1021/ja405874t | J. Am. Chem. Soc. 2013, 135, 15467–15478

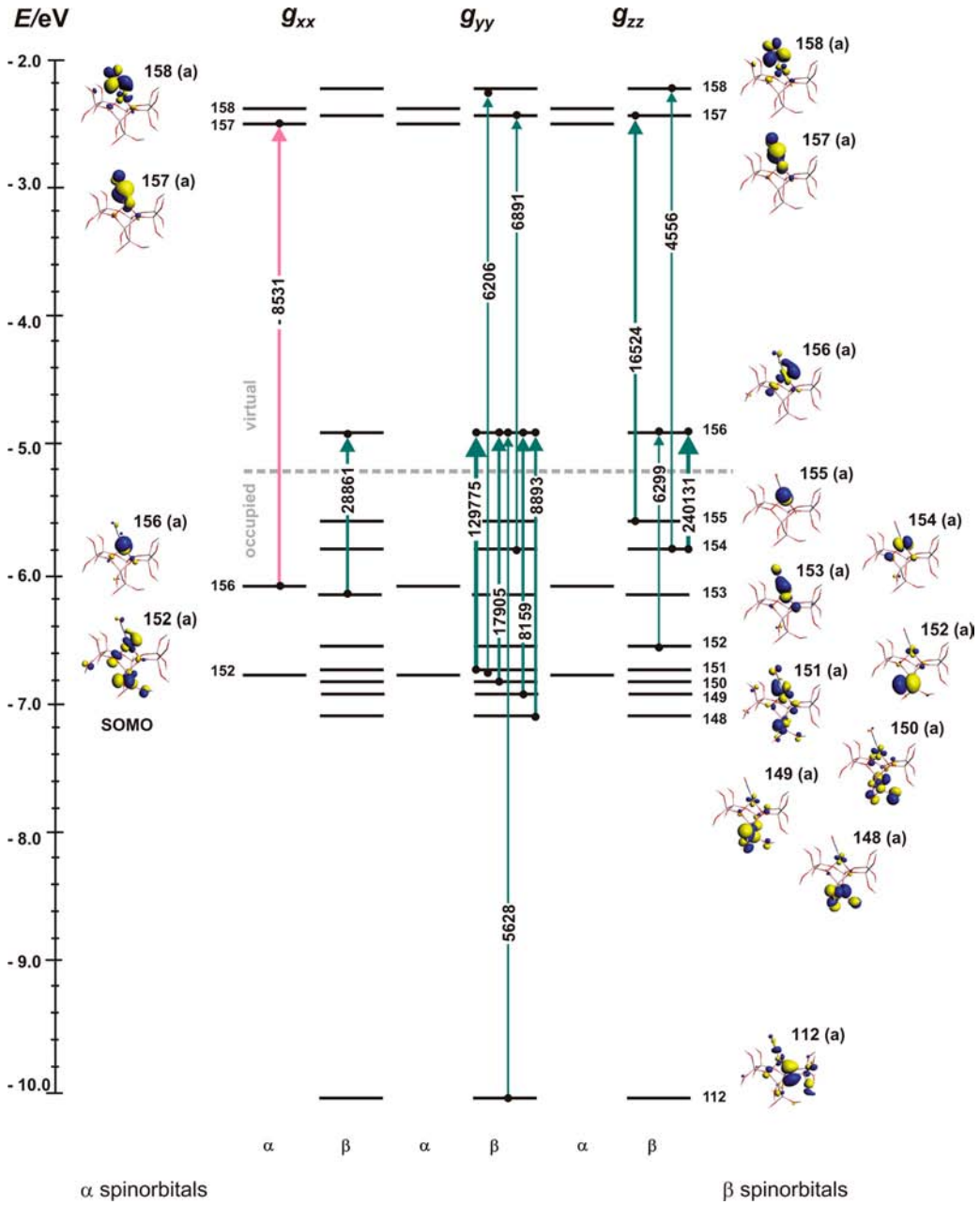

Figure 6. Kohn–Sham orbital diagram for the most important paramagnetic contributions to the g tensor components of the {Ni^{I}–CO}**M7** cluster in the spin-unrestricted BP/TZP scalar relativistic calculations based on the Pauli Hamiltonian. The magnetic field-induced couplings (transitions) are indicated with arrows, whereas the values of the corresponding contributions to Δg_{ii} (>15% of g_{iso}) are given in ppm.

hosted in the ZSM-5, $[Ni^{I}_{4c}\mathbf{M7}]_{frag}$, and the bidentate nickel site in a virtual entatic state, pro-adduct $[Ni^{I}_{2c}\mathbf{M7}]_{frag}$, corresponding to the actual coordination environment of the nickel moiety in the {Ni^{I}–CO}**M7** adduct with removed CO ligand. Since upon interaction with CO the coordination state of nickel(I) changes dramatically from the planar 4-fold to the T-shaped trigonal one, such a three-fragment approach leads to a more transparent picture of the CO bonding, reducing a complicated mixing of many orbitals to few key interactions between the meaningful FMO. The ensuing orbital overlap correlation diagram of the π(2p) and σ states of the carbon monoxide ligand with the 3d states of the $[Ni^{I}_{2c}\mathbf{M7}]_{frag}$ fragment referenced to the states of the parent Ni^{I}_{4c}**M7** cluster is shown in Figure 5.

In the $[Ni^{I}_{2c}\mathbf{M7}]_{frag}$ pro-adduct state, the change in the nickel coordination results in a significant alteration of the 3d energy. The position of the **146**($3d_{yz}$) level of the Ni^{I}**M7** cluster drops by 1.3 eV, making it energetically more accessible for interaction with the CO out-of-plane **5**($\pi_y(2p_y)$) orbital, whereas that of **147**($3d_{xz}$) one, of the same symmetry as the CO in-plane **6**($\pi_x(2p_x)$) state, is almost unchanged. Essentially, the binding of CO results from the π overlap between low-laying π(2p) CO states with the symmetry adopted $3d_{xz}$ and $3d_{yz}$ orbitals of nickel. It is further enhanced by a small contribution due to the σ overlap between **7**(σ(2p+2s)) and one of the lobes of the in-plane **149**($3d_{xz}$) orbital, produced by the unusual T-shape geometry of the (OC)–Ni–$(O_{(Al)})_2$ unit. The low-laying **109**α and **107**α, **108**β and **107**β bonding spin orbitals have their antibonding **158**α and **157**α, **158**β and **157**β

dx.doi.org/10.1021/ja405874t | J. Am. Chem. Soc. 2013, 135, 15467–15478

counterparts that contribute to the magnetic couplings responsible for the pronounced g tensor anisotropy, discussed in the next section in more detail.

The energy levels of the bonding and antibonding $\pi(2p)$ CO orbitals define the low and high-energy boundaries encompassing the 3d nickel-based **145**−**149** states of the $[Ni^{I}_{2c}\mathbf{M7}]_{frag}$ pro-adduct. These states, being essentially nonbonding with respect to the zeolite framework, generally remain also nonbonding in the $\{Ni^{I}-CO\}\mathbf{M7}$ adduct. They are yet modulated by tiny contributions coming from the π^*_x and π^*_y states of CO, giving rise to **152**α and **156**β, **153**α, and **153**β orbitals, respectively. Thus, the interaction of the **145**−**149** 3d states with the corresponding CO orbitals results in a strong spin-polarization, reflected by the pronounced shift of the α and β spin manifolds of the $\{Ni^{I}-CO\}\mathbf{M7}$ species, and the changes in their energy ordering (compare the occupied **152**α and the virtual **156**β states of the same symmetry, Figure 5). The singly occupied **152**α orbital exhibits little delocalization on the CO moiety, which nicely explains the lack of the ^{13}C hyperfine splitting in the CW-EPR spectra (Figure 1b, dotted line). The residual spin density seen in Figure 2c accounts well for the very weak hyperfine interaction detected in the HYSCORE experiments (as explained above). Although the **147**−**156** orbitals of the $\{Ni^{I}-CO\}\mathbf{M7}$ adduct do not contribute directly to the binding of CO to the zeolite nickel(I) sites, they are of fundamental importance for explaining the experimentally observed increase of the g tensor anisotropy with respect to the parent tetracoordinated Ni^{I} sites (Figure 1a,b), explained below thoroughly.

3.4. DFT Account of {Ni^{I}−CO} Spectroscopic Features. According to the partitioning scheme implied by the scalar Pauli Hamiltonian approach,[53] the components of the experimental g tensor ($g_{ij} = g_e + \Delta g_{ij}$) can be rationalized in terms of the individual molecular orbital contributions to the particular g_{ij} values: $\Delta g_{ij} = \Delta g^{rel}_{ij} + \Delta g^{d}_{ij} + \Delta g^{p}_{ij}$, where Δg^{rel}_{st} combines scalar relativistic corrections, whereas the terms Δg^{d}_{st} and Δg^{p}_{st} stand for dia- and paramagnetic contributions to Δg, respectively. The paramagnetic term (Δg^{p}_{st}) dominates deviation of the g tensor elements from the free-electron value (g_e). It contains the contributions due to a frozen core ($\Delta g_{st}^{p,core}$), a magnetic field-induced coupling between the occupied orbitals ($\Delta g_{st}^{p,occ-occ}$), and the occupied and the virtual magnetic orbitals ($\Delta g_{st}^{p,occ-virt}$). It has been shown that $\Delta g_{ij}^{p,occ-virt}$ governs the paramagnetic term (and, as a consequence, the total Δg_{ij} shift) for transition metal complexes,[53] including nickel(I) adducts.[24,27] Therefore, while discussing the molecular nature of the g tensor anisotropy for the $\{Ni^{I}-CO\}\mathbf{M7}$ adduct, we may reasonably confine our description to this overwhelming term only.

The principal magnetic couplings to the g_{ij} components of the nickel(I) monocarbonyl adduct within the spin-unrestricted resolution are shown in Figure 6, along with the contours of the corresponding magnetic orbitals. Because of the C_1 point symmetry of the $\{Ni^{I}-CO\}\mathbf{M7}$ species, all possible couplings specified by the following integrals are allowed:[63]

$$\Delta g_{ij}^{p,occ-virt} \propto \frac{1}{2c(\varepsilon^{\sigma}_{virt} - \varepsilon^{\sigma}_{occ})} \langle \Psi^{\sigma}_{virt} | iL_{x,y,z} | \Psi^{\sigma}_{occ} \rangle \quad (3)$$

where Ψ_{occ} and Ψ_{virt} represent the occupied and the virtual unperturbed Kohn−Sham orbitals, respectively, ε is one-electron energy of these orbitals, L is the orbital momentum operator, whereas σ stands for α or β spin. To simplify the diagram, only the most important contributions (above 15% of the Δg_{iso} value) are shown. For the sake of further discussion the Ψ_{occ} and Ψ_{virt} states can be classified as the metal-based and ligand-based spin orbitals.

The small positive shift of the g_{xx} component with respect to g_e value can be explained by a single metal−ligand positive coupling defined by the β-**153**$a(d_{yz} + \pi^*_{y,CO}) \leftrightarrow \beta$-**156**$a(d_{xz} + \pi^*_{x,CO})$ transition induced by the magnetic field, which is attenuated by the negative α-**156**$a(d_{y^2}) \leftrightarrow \alpha$-**157**$a(d_{yz} + \pi^*_{y,CO})$ component. Note that the β-**156**$a(d_{xz} + \pi^*_{x,CO})$ orbital is an empty counterpart of the α-**152**a SOMO state, and that it is mostly involved in all g_{ii} components.

The high anisotropy of the g tensor, reflected by large positive shift of the g_{zz} ($\Delta g_{zz} = 0.434$) value, results mainly from the dominant β-**154**$a(d_{x^2-y^2}) \leftrightarrow \beta$-**156**$a(d_{xz} + \pi^*_{x,CO})$ coupling. This major contribution is associated with its specific metal-to-metal character, small energy separation of the involved states, and large spin−orbit coupling constant ($\xi = 605\ cm^{-1}$) of the nickel(I) core. It is additionally reinforced by three weaker β-**152**$a(d_{xz} + L_{zeol}) \leftrightarrow \beta$-**156**$a(d_{xz} + \pi^*_{x,CO})$, β-**154**$a(d_{x^2-y^2}) \leftrightarrow \beta$-**158**$a(d_{xz} - \pi^*_{x,CO})$, and β-**155**$a(d_{y^2}) \leftrightarrow \beta$-**157**$a(d_{yz} - \pi^*_{y,CO})$ magnetic transitions. All of them exhibit mostly the metal-to-ligand character, and by involving energetically strongly separated states are of less impact.

In the case of the g_{yy} component, the number of transitions increases to seven (Figure 6), leading to a complex coupling scheme. However, the most important β-**151**$a(d_{xz} + d_{yz} + \pi^*_{x,CO}) \leftrightarrow \beta$-**156**$a(d_{xz} + \pi^*_{x,CO})$ transition along with the combinations of the β-**150**a, β-**149**a, and β-**148**a magnetic orbitals, all coupled to β-SOMO **156**$a(d_{xz} + \pi^*_{x,CO})$, exhibit a strong metal-to-metal character, and therefore give rise to the large Δg_{yy} shift. It is further enhanced by the β-**151**$a(d_{xz} + d_{yz} + \pi^*_{x,CO}) \leftrightarrow \beta$-**158**$a(d_{xz} - \pi^*_{x,CO})$ and β-**154**$a(d_{x^2-y^2}) \leftrightarrow \beta$-**157**$a(d_{yz} - \pi^*_{y,CO})$ transitions involving antibonding π^* states of the CO ligand. Consequently, the resultant coupling scheme provides with the unprecedented accuracy a detailed rigorous molecular rational for the $g_{zz} > g_{yy} \gg g_{xx}$ sequence that is actually observed in the CW-EPR experiment.

The already mentioned red shift $\Delta\nu = -34\ cm^{-1}$ of the C−O stretching frequency with respect to the gas-phase carbon monoxide (Figure 1c) can be accounted for by the electron population analysis obtained from DFT calculations. It was found that upon ligation the CO molecule acquires a negative charge ($q_{CO} = -0.04$), whereas the Ni center becomes oxidized ($\Delta q_{Ni} = +0.05$) with respect to the bare $Ni^{I}\mathbf{M7}$ site. The partial charge redistribution within the $\{Ni^{I}-CO\}$ unit arises from the balance between the ligand-to-metal (donation) and the metal-to-ligand (back-donation) flows of the electron density between the interacting moieties. In the classic description of the electron repartition for the metal carbonyl adducts,[64] σ donation results in a slight increase of the CO stretching frequency (since the σ lone pair of CO is partially antibonding), which can be enhanced further by the electrostatic interactions.[15] The π back-donation effect provides the mechanism of decreasing the stretching frequency with respect to that of gas-phase CO due to the partial population of the $\pi^*(2p)$ orbitals. This delicate balance between the donation and the back-donation effects was quantified by means of the ETS-NOCV analysis, and the specific charge and spin flow channels were identified and arranged in terms of their energetic relevance. Within the assumed decomposition scheme into the $[CO]_{frag}$ and $[Ni^{I}_{2c}\mathbf{M7}]_{frag}$ fragments, the interaction energy can be factored into the electrostatic (ΔE_{elect}), steric (ΔE_{steric}), and orbital (ΔE_{orb}) contributions following Moro-

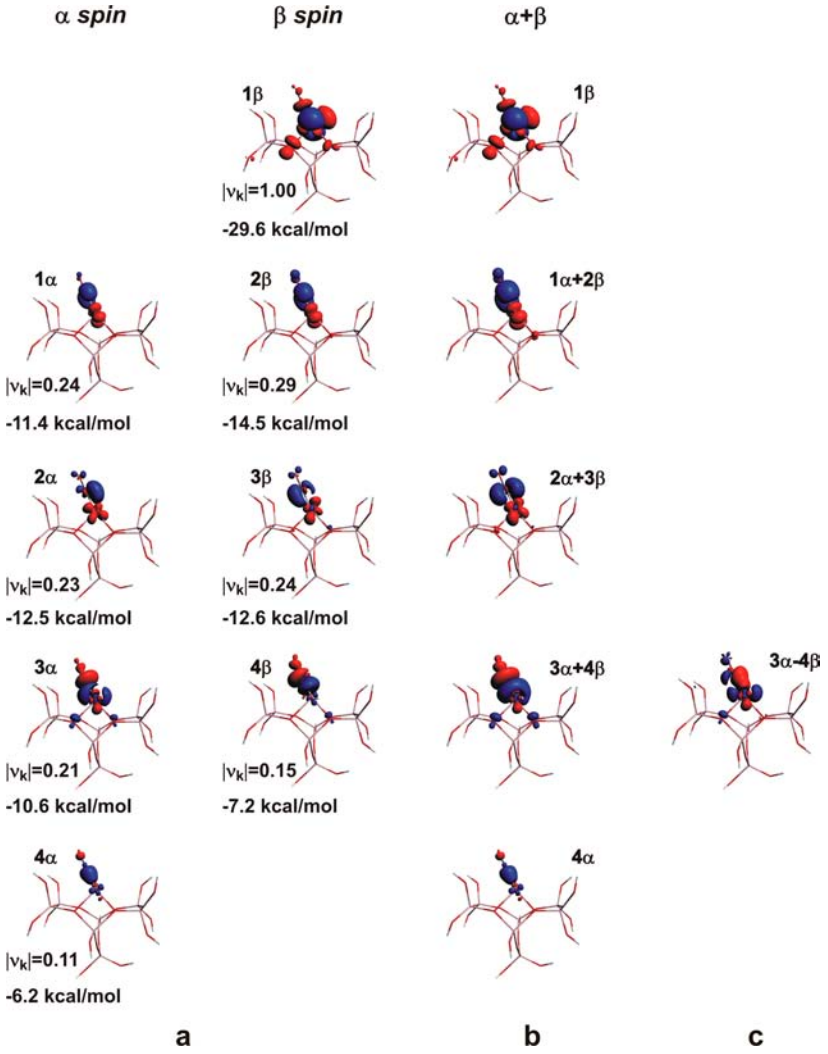

Figure 7. NOCV deformation density contours revealing electron density flow channels between interacting $[Ni^{I}_{2c}\mathbf{M7}]_{frag}$ and $[CO]_{frag}$ fragments (a) in spin unrestricted resolution, (b) total electron density ($\alpha + \beta$) contours and (c) spin density ($\alpha - \beta$) contour for $3\alpha + 4\beta$ channel. The corresponding values indicate interaction energies characteristic of the individual channels. Blue and red shading corresponds to gain and loss of the electron (spin) density, respectively.

kuma–Ziegler partitioning.[65] The ΔE_{steric} part arises from the Pauli repulsive interaction (+158 kcal/mol) between the closed shell orbitals of both fragments and the attractive electrostatic interaction $\Delta E_{elect} = -123$ kcal/mol. The overall constructive binding effect is assured by the substantial orbital component, $\Delta E_{orb} = -105$ kcal/mol, which can be next divided into the specific interaction channels. The main orbital contributions ($|\nu_k| > 0.1$) to the α and β electron and spin density flows constituting those channels are shown in Figure 7, along with the corresponding energy values.

Using local symmetry arguments, the overlapping orbitals may be categorized into the σ and π channels. The π channels are formed by two pairs of the spin orbitals, $1\alpha + 2\beta$ and $2\alpha + 3\beta$, involving two perpendicular π^*_y and π^*_x molecular orbitals of the CO ligand, respectively. Since both α and β spin manifolds are nearly equally involved herein, these channels can be identified with the spinless charge transfer process. The π channel is implicated in the back-donation charge transfer from $3d_{yz}$ to π^*_y ($1\alpha + 2\beta$) and from $3d_{xz}$ to π^*_x ($2\alpha + 3\beta$) orbitals. This electron density flow is responsible for the lowering of the CO stretching frequency.

The σ donation channel is constituted by the $3\alpha + 4\beta$ pair of the spin orbitals, giving rise to the cooperative charge transfer from the CO ligand to the 3d orbitals of nickel (mainly $3d_{xz}$ and $3d_{z^2}$), associated with a moderate energy gain (−17.8 kcal/mol). This channel is slightly augmented by another σ channel (4α), yet of a very small energy (−6.2 kcal/mol), operating only within the α spin states (consistent thereby with a congruent spin and charge transfer), which leads to a very small spin density on the CO ligand. As a result, the sum of the individual contributions to the energy due to the orbital interaction along the π channels (−50 kcal/mol) dominates the effects arising from the σ channels (−24 kcal/mol), which explains the observed distinct bathochromic CO stretching frequency shift.

The congruent rearrangement of the β-spin and charge, observed for the 1β channel, can be interpreted as a relaxation process involving the $3d_{xz}$ and $3d_{y^2}$ nickel-based orbitals induced by CO ligation. The entatic $[Ni^{I}_{2c}\mathbf{M7}]_{frag}$ reference fragment represents the state of enhanced energy, which upon interaction with CO not only allows for electron density redistribution within the σ and π channels, but also involves appropriate rearrangement of 3d levels (Figure 5), reflected by

dx.doi.org/10.1021/ja405874t | J. Am. Chem. Soc. 2013, 135, 15467−15478

one electron flip between 3d orbitals (vide $|\nu_k| = 1$ for 1β). The latter one is referred to as a metal orbital relaxation process.

As a result, the applied ETS-NOCV analysis allowed for disentangling and quantification of the cooperative σ donation and π back-donation effects involved in the binding of CO to nickel(I). Indeed, the dominant contribution arises from the back-donation π channel of spinless charge transfer. This explains the position of the carbonyl band in the experimental IR spectrum (Figure 1c), and its bathochromic frequency shift with respect to the free CO molecule. The spin density redistribution within the CO moiety operates mainly via 4α and $3\alpha + 4\beta$ σ channels. Because of the significantly unequal contributions of the 3α and 4β components, the resultant unbalanced spin flow (Figure 7c) gives rise to a spin polarization of the carbon sp hybrid. On the contrary, the 4α channel allows for a direct delocalization of the spin density onto the carbon 2s orbital. Yet, the polarization effect dominates that of the direct delocalization, which nicely rationalizes the negative sign of the isotropic constant $a_{iso}(^{13}C)$, and consequently the convention of the signs for the $A_{ii}(^{13}C)$ components assumed in the HYSCORE simulations (Table 1). Being of opposite sign, those two effects lead to a very small total spin density flow within the σ channel. The dipolar ^{13}C $\boldsymbol{T}$ tensor shows, in turn, a noticeable rhombic symmetry. Accordingly, it can be decomposed into two axially symmetric contributions along the z and y directions as follows: $[\boldsymbol{T}]_{ii}$/MHz = [2.4; −2.2; −0.2] = [0.87; 0.87; −1.74] + [1.53; −3.06; 1.53]. The estimated proportion of the $2p_z$ and $2p_y$ spin densities obtained from the principal values of both axial tensors (0.87 and 1.53, respectively) agrees well with the Mulliken population analysis ($\rho(2p_z) = -0.015$, $\rho(2p_y) = -0.028$ and $\rho(2p_x) = 0.000$) since $0.87/1.53 \approx 0.015/0.028$.

Since upon CO ligation the unpaired electron relaxation process (1β) is restricted to the nickel-based 3d orbitals only, and the main channels (one σ and two π) of the electron density flow within the {Ni^{I}−CO} unit involve both α and β spins in a similar way, the magnetophore part of the adduct is largely confined to the metal core (Figure 2c). All those effects provide the basis for the unique molecular account of the observed IR and EPR parameters in terms of the incommensurate charge and spin flows.

4. CONCLUSIONS

By means of combined use of CW-EPR, HYSCORE, and IR spectroscopies using isotopically enriched carbon-13 CO adsorption and comprehensive DFT molecular modeling it was demonstrated that interaction of carbon monoxide with Ni^{I}ZSM-5 zeolite under low pressures leads to formation of the top-on (η^1) monocarbonyl adduct of trigonal nickel(I). The EPR parameters with $g_{zz} > g_{yy} \gg g_{xx} > g_e$, $|A_{yy}| > |A_{zz}| > |A_{xx}|$ are characteristic of the T-shaped conformation. The ligation of CO is accompanied by the strong internal d−d relaxation of the metal core due to the joint charge and β-spin relocation between the $3d_{xz}$ and $3d_{y^2}$ orbitals, stabilizing the adduct energetically. On the basis of the spectroscopic constraints (ν_{CO} and $\boldsymbol{g}$, $\boldsymbol{A}(^{13}C)$, $\boldsymbol{Q}(^{27}Al)$ tensors) refined with DFT modeling a complete model of the electronic and magnetic structure of the adduct was developed. The spectroscopic parameters (g_{xx} = 2.018, g_{yy} = 2.380, g_{zz} = 2.436, A_{xx} = +1.0 MHz, A_{yy} = −3.6 MHz, A_{zz} = −1.6 MHz for ^{13}C hyperfine interaction, and e^2Qq/h = −13 MHz, η = 0.8 for ^{27}Al quadrupole interaction) obtained by computer simulations of the EPR and HYSCORE spectra and reinforced with DFT calculations with the ZORA-SOMF/B3LYP scheme definitely validate the proposed η^1 T-shaped structure of the {Ni^{I}−CO} intrazeolite adduct. Detailed molecular nature of the $\boldsymbol{g}$ tensor was rationalized in terms of the magnetic field-induced couplings of the molecular orbitals using the scalar relativistic Pauli Hamiltonian. The disentangled charge and spin flows within the {Ni^{I}−CO} magnetophore along the orbital channels of σ and π symmetry were quantified be means of the ETS-NOCV method. The observed bathochromic shift of the C−O stretching frequency (IR) resulted from the dominant spinless in-plane and out-of-plane π back-donation charge transfer (−50 kcal/mol), while incongruent spin and charge transfer via the σ channel (−24 kcal/mol) is responsible for the spin delocalization and spin polarization processes (EPR, HYSCORE).

■ ASSOCIATED CONTENT

Supporting Information

Simulation of ^{27}Al HYSCORE spectra and table with spectral parameters, computational details, calculation results for the additional models of the monocarbonyls, geometries of the optimized structures in Cartesian coordinates. This material is available free of charge via the Internet at http://pubs.acs.org.

■ AUTHOR INFORMATION

Corresponding Author

pietrzyk@chemia.uj.edu.pl

Notes

The authors declare no competing financial interest.

■ ACKNOWLEDGMENTS

Financial support for the research from the Ministry of Science and Higher Education (MNiSW) of Poland, Grant No. Iuventus Plus IP2011 041871, is acknowledged. T.M. thanks the International PhD studies program within the MPD Program of Foundation for Polish Science cofinanced by the EU Regional Development Fund for supporting his stay at the University of Turin. K.P.-S. is thankful for the postdoc position from the "Society−Environment−Technologies" project at the Jagiellonian University in the framework of the EU Social Fund. The calculations were carried out with the computer facilities of Academic Computing Centre CYFRONET-AGH under Grant No. MNiSW/IBM_BC_HS21/UJ/092/2008. The research was carried out with the equipment purchased thanks to the financial support of the European Regional Development Fund in the framework of the Polish Innovation Economy Operational Program (Contract No. POIG.02.01.00-12-023/08). We dedicate this paper to Professor Michel Che (Université Pierre et Marie Curie, Paris 6, France) honoring the golden jubilee of his scientific and academic activity.

■ REFERENCES

(1) Costa, D.; Martra, G.; Che, M.; Manceron, L.; Kermarec, M. *J. Am. Chem. Soc.* **2002**, *124*, 7210−7217.

(2) Aleksandrov, H. A.; Zdravkova, V. R.; Mihaylov, M. Y.; St. Petkov, P.; Vayssilov, G. N.; Hadjiivanov, K. I. *J. Phys. Chem. C* **2012**, *116*, 22823−22831.

(3) Lupinetti, A. J.; Strauss, S. H.; Frenking, G. *Prog. Inorg. Chem.* **2001**, *49*, 1−112.

(4) Zhou, M. F.; Andrews, L.; Bauschlicher, C. W. *Chem. Rev.* **2001**, *101*, 1931−1962.

(5) Mosqueda-Jiménez, B. I.; Jentys, A.; Seshan, K.; Lercher, J. A. *J. Catal.* **2003**, *218*, 375−385.

(6) Craft, J. L.; Mandimutsira, B. S.; Fujita, K.; Riordan, C. G.; Brunold, T. C. *Inorg. Chem.* **2002**, *42*, 859−867.
(7) Lepage, M.; Visser, T.; Soulimani, F.; Beale, A. M.; Iglesias-Juez, A.; Van Der Eerden, A. M. J.; Weckhuysen, B. M. *J. Phys. Chem. C* **2008**, *112*, 9394−9404.
(8) Qi, G.; Xu, J.; Su, J.; Chen, J.; Wang, X.; Deng, F. *J. Am. Chem. Soc.* **2013**, *135*, 6762−6765.
(9) Wang, V. C.-C.; Can, M.; Pierce, E.; Ragsdale, S. W.; Armstrong, F. A. *J. Am. Chem. Soc.* **2013**, *135*, 2198−2206.
(10) Wang, W.-J.; Lin, H.-Y.; Chen, Y.-W. *J. Porous Mater.* **2005**, *12*, 5−12.
(11) Naknama, P.; Luengnaruemitchai, A.; Wongkasemjit, S.; Osuwan, S. *J. Power Sources* **2007**, *165*, 353−358.
(12) Bernardo, P.; Algieri, C.; Barbieri, G.; Drioli, E. *Sep. Purif. Technol.* **2008**, *62*, 629−635.
(13) Hadjiivanov, K.; Knözinger, H.; Mihaylov, M. *J. Phys. Chem. B* **2002**, *106*, 2618−2624.
(14) Hadjiivanov, K. I.; Vayssilov, G. N. *Adv. Catal.* **2002**, *47*, 307−511.
(15) Otero Arean, C.; Tsyganenko, A. A.; Escalona Platero, E.; Garrone, E.; Zecchina, A. *Angew. Chem., Int. Ed.* **1998**, *37*, 3161−3163.
(16) Dorado, F.; de Lucas, A.; Garcia, P. B.; Romero, A.; Valverde, J. L.; Asencio, I. *Ind. Eng. Chem. Res.* **2005**, *44*, 8988−3996.
(17) Mlinar, A. N.; Baur, G. B.; Bong, G. G.; Getsoian, A.; Bell, A. T. *J. Catal.* **2012**, *296*, 156−164.
(18) Fakeeha, A. H.; Al-Fatesh, A. S.; Abasaeed, A. E. *Adv. Mater. Res.* **2012**, *550*−*553*, 325−328.
(19) Harrop, T. C.; Mascharak, P. K. *Coord. Chem. Rev.* **2005**, *249*, 3007−3024.
(20) Grochala, W. *Phys. Chem. Chem. Phys.* **2006**, *8*, 1340−1345.
(21) Eckert, N. A.; Dinescu, A.; Cundari, T. R.; Holland, P. L. *Inorg. Chem.* **2005**, *44*, 7702−7704.
(22) Frey, M. *Struct. Bonding (Berlin, Ger.)* **1998**, *90*, 97−126.
(23) Bennett, B.; Lemon, B. J.; Peters, J. W. *Biochemistry* **2000**, *39*, 7455−7460.
(24) Pietrzyk, P.; Podolska, K.; Sojka, Z. *Chem.—Eur. J.* **2009**, *15*, 11802−11807.
(25) Alvarez, S. *Coord. Chem. Rev.* **1999**, *193*−*195*, 13−41.
(26) Moncho, S.; Ujaque, G.; Lledos, A.; Espinet, P. *Chem.—Eur. J.* **2008**, *14*, 8986−8994.
(27) Pietrzyk, P.; Podolska, K.; Mazur, T.; Sojka, Z. *J. Am. Chem. Soc.* **2011**, *133*, 19931−19943.
(28) Neese, F.; Munzarova, M. L. In *Calculation of NMR and EPR Parameters. Theory and Applications*; Kaupp, M., Bühl, M., Malkin, V. G., Eds.; Wiley-VCH: Weinheim, Germany, 2004; p 21.
(29) Pietrzyk, P.; Podolska, K.; Sojka, Z. *Electron Paramagn. Reson.* **2013**, *23*, 264−311.
(30) Stadler, C.; de Lacey, A. L.; Hernandez, B.; Fernandez, V. M.; Conesa, J. C. *Inorg. Chem.* **2002**, *41*, 4417−4423.
(31) Ray, K.; Weyhermuller, T.; Neese, F.; Wieghardt, K. *Inorg. Chem.* **2005**, *44*, 5345−5360.
(32) Stein, M.; van Lenthe, E.; Baerends, E. J.; Lubitz, W. *J. Phys. Chem. A* **2001**, *105*, 416−425.
(33) Sojka, Z.; Pietrzyk, P.; Martra, G.; Kermarec, M.; Che, M. *Catal. Today* **2006**, *115*, 154−161.
(34) Pietrzyk, P.; Podolska, K.; Sojka, Z. *J. Phys. Chem. A* **2008**, *112*, 12208−12219.
(35) Page, M. J.; Lu, W. Y.; Poulten, R. C.; Carter, E.; Algarra, A. G.; Kariuki, B. M.; MacGregor, S. A.; Mahon, M. F.; Cavell, K. J.; Murphy, D. M.; Whittlesey, M. K. *Chem.—Eur. J.* **2013**, *19*, 2158−2167.
(36) Spalek, T.; Pietrzyk, P.; Sojka, Z. *J. Chem. Inf. Model.* **2005**, *45*, 18−29.
(37) Höfer, P.; Grupp, A.; Nebenfür, H.; Mehring, M. *Chem. Phys. Lett.* **1986**, *132*, 279−282.
(38) (a) Stoll, S.; Schweiger, A. *J. Magn. Reson.* **2006**, *178*, 42−55. (b) Stoll, S.; Britt, R. D. *Phys. Chem. Chem. Phys.* **2009**, *11*, 6614−6625.
(39) Mentzen, B. F.; Bergeret, G. *J. Phys. Chem. C* **2007**, *111*, 12512−12516.
(40) Groothaert, M. H.; Pierloot, K.; Delabie, A.; Schoonheydt, R. A. *Phys. Chem. Chem. Phys.* **2003**, *5*, 2135−2144.
(41) Pietrzyk, P.; Sojka, Z. *J. Phys. Chem. A* **2005**, *109*, 10571−10581.
(42) Pietrzyk, P.; Podolska, K.; Sojka, Z. *J. Phys. Chem. C* **2011**, *115*, 13008−13015.
(43) Frisch, M. J.; Trucks, G. W.; Schlegel, H. B.; Scuseria, G. E.; Robb, M. A.; Cheeseman, J. R.; Scalmani, G.; Barone, V.; Mennucci, B.; Petersson, G. A.; Nakatsuji, H.; Caricato, M.; Li, X.; Hratchian, H. P.; Izmaylov, A. F.; Bloino, J.; Zheng, G.; Sonnenberg, J. L.; Hada, M.; Ehara, M.; Toyota, K.; Fukuda, R.; Hasegawa, J.; Ishida, M.; Nakajima, T.; Honda, Y.; Kitao, O.; Nakai, H.; Vreven, T.; Montgomery, Jr., J. A.; Peralta, J. E.; Ogliaro, F.; Bearpark, M.; Heyd, J. J.; Brothers, E.; Kudin, K. N.; Staroverov, V. N.; Kobayashi, R.; Normand, J.; Raghavachari, K.; Rendell, A.; Burant, J. C.; Iyengar, S. S.; Tomasi, J.; Cossi, M.; Rega, N.; Millam, J. M.; Klene, M.; Knox, J. E.; Cross, J. B.; Bakken, V.; Adamo, C.; Jaramillo, J.; Gomperts, R.; Stratmann, R. E.; Yazyev, O.; Austin, A. J.; Cammi, R.; Pomelli, C.; Ochterski, J. W.; Martin, R. L.; Morokuma, K.; Zakrzewski, V. G.; Voth, G. A.; Salvador, P.; Dannenberg, J. J.; Dapprich, S.; Daniels, A. D.; Farkas, Ö.; Foresman, J. B.; Ortiz, J. V.; Cioslowski, J.; Fox, D. J. *Gaussian 09*, Revision A.02; Gaussian, Inc.: Wallingford, CT, 2009.
(44) Becke, A. D. *J. Chem. Phys.* **1993**, *98*, 5648−5652.
(45) (a) McLean, A. D.; Chandler, G. S. *J. Chem. Phys.* **1980**, *72*, 5639−48. (b) Wachters, A. J. H. *J. Chem. Phys.* **1970**, *52*, 1033−1036.
(46) Li, X.; Frisch, M. J. *J. Chem. Theory Comput.* **2006**, *2*, 835−839.
(47) Mitoraj, M.; Michalak, A. *J. Mol. Model.* **2007**, *13*, 347−355.
(48) Michalak, A.; Mitoraj, M.; Ziegler, T. *J. Phys. Chem. A* **2008**, *112*, 1933−1939.
(49) te Velde, G.; Bickelhaupt, F. M.; Baerends, E. J.; Fonseca Guerra, C.; van Gisbergen, S. J. A.; Snijders, J. G.; Ziegler, T. *J. Comput. Chem.* **2001**, *22*, 931−967.
(50) *ADF2009.01, SCM, Theoretical Chemistry*; Vrije Universiteit: Amsterdam; http://www.scm.com.
(51) Neese, F. *ORCA—An ab initio, Density Functional and Semiempirical Program Package*, Version 2.8; Lehrstuhl für Theoretische Chemie: Bonn, Germany, 2011.
(52) Neese, F. *J. Chem. Phys.* **2001**, *115*, 11080−11096.
(53) Schreckenbach, G.; Ziegler, T. *J. Phys. Chem. A* **1997**, *101*, 3388−3399.
(54) Neese, F. *J. Chem. Phys.* **2003**, *118*, 3939−3948.
(55) Neese, F. *Inorg. Chim. Acta* **2002**, *337C*, 181−192.
(56) Kieber-Emmons, M. T.; Riordan, C. G. *Acc. Chem. Res.* **2007**, *40*, 618−625.
(57) Góra-Marek, K.; Glanowska, A.; Datka, J. *Microporous Mesoporous Mater.* **2012**, *158*, 162−169.
(58) Bonnevoit, L.; Olivier, D.; Che, M. *J. Mol. Catal.* **1983**, *21*, 415−430.
(59) Freude, D.; Klinowski, J.; Hamdan, H. *Chem. Phys. Lett.* **1988**, *149*, 355−362.
(60) Hunger, M.; Horvath, T. *J. Am. Chem. Soc.* **1996**, *118*, 12302−12308.
(61) Mabbs, F. E.; Collison, D. *Electron Paramagnetic Resonance of d Transition Metal Compounds*; Elsevier: Amsterdam, 1992; p 427.
(62) Goodman, B. A.; Raynor, J. B. Electron spin resonance of transition metal complexes. In *Advances in Inorganic Chemistry and Radiochemistry*; Emeléus, H. J., Sharpe, A. G., Eds; Academic Press: New York, 1970; Vol. *13*, pp 135−362.
(63) Schreckenbach, G.; Ziegler, T. *J. Phys. Chem.* **1995**, *99*, 606−611.
(64) Lupinetti, A. J.; Fau, S.; Frenking, G.; Strauss, S. H. *J. Phys.Chem. A* **1997**, *101*, 9551−9559.
(65) Bickelhaupt, F. M.; Baerends, E. J. In *Reviews in Computational Chemistry*; Lipkowitz, K. B., Boyd, D. B., Eds.; Wiley-VCH: New York, 2000; Vol. *15*, pp 1−86.